Theoretical Position-Velocity Diagrams of Flux, Electron Density, and Electron Temperature in Herbig-Haro Objects

Rémy Indebetouw

Maria Mitchell Observatory

3 Vestal St., Nantucket, MA 02554

email: rindebet@maria1.mmo.org

and

Alberto Noriega-Crespo

Maria Mitchell Observatory

3 Vestal St., Nantucket, MA 02554

and

Infrared Processing and Analysis Center

California Institute of Technology, Jet Propulsion Laboratory

Pasadena, CA 91125

email: alberto@ipac.caltech.edu

Received _____; accepted _____

ABSTRACT

Many features of Herbig-Haro objects can be reproduced using a kinematical bow shock model. We use the model to generate position-velocity (PV) diagrams of flux in H_α, [O I]$\lambda\lambda$6300+63, [S II]$\lambda\lambda$6716+31, [O III]$\lambda\lambda$4959+5007, and [C I]$\lambda\lambda$9823+50, line ratios of [O I]/H_α, [O I]/[S II], [S II]/H_α, H_α/[S II], and [O III]/H_α, electron density N_e, and electron temperature T_e. We show how position-velocity diagrams of N_e and flux vary with shock kinematics. By matching PV diagrams with observation, we have determined a narrow range of parameters for HH 1F, 2(A′+H), and 43(B+C). We can use line ratios and N_e (determined from a line ratio) to narrow the possible range of shock parameters. We model the N_e features of HH 2(A′+H) as a superposition of 2 bowshocks. We also show that the effects of slight misalignments of the two diagrams to be divided can produce artifacts in line ratios and N_e which obliterate the physical features. We show that N_e in HH 1 can only be explained using the kinematical model by taking these misalignments in to account.

1. Introduction

Herbig-Haro (HH) objects and stellar jets trace the interaction of the outflowing matter from young stellar objects in their evolution towards the main sequence (Shu, Adams & Lizano 1987). This interaction is through shocks, gas from the proto-stellar object and/or its accretion disk strikes its surrounding medium (Schwartz 1975). The shocks manifest themselves in strong Balmer, forbidden (e.g. [S II] 6717/31, [O I] 6300/63, [O III]5007) and molecular (e.g. H_2 2.121 μm) emission lines. Some of the brightest HH objects correspond to the leading working surfaces of the jets (Herbig & Jones 1981; Mundt 1987; Raga 1988; Hartigan 1989) and it has been possible to study their properties to a first approximation with relatively simple kinematical models of bowshock structures (Choe, Böhm & Solf 1985; Raga & Böhm 1985; Hartigan, Raymond & Hartmann 1987, hereafter HRH87). The kinematical bowshock model assumes that for every point in its structure the emission can be modeled by a plane parallel shock model. Its advantage, with respect the present hydrodynamical models (Blondin, Königl & Fryxell 1989; Stone & Norman 1993; Raga 1994), is that it includes the more detailed physics that is achieved in one-dimensional shock models. The kinematical models have helped to understand some of the HH working surface spectroscopic observations (Solf, Böhm & Raga 1986; HRH87), their electron density and temperature distributions (Noriega-Crespo, Raga & Böhm 1989, 1990), some features in the spatially resolved spectra (Solf, Böhm & Raga 1988; Solf and Böhm 1991), and the morphology and spectral characteristics of their molecular hydrogen emission (Curiel, Raymond & Hartigan 1994; Smith & Brand 1990; Smith, Brand & Moorhouse 1991).

In this study we consider a more detailed comparison between the bow shock models and some recent spatially resolved spectroscopic observations that show some unusual morphological features (Solf & Böhm 1991). The goal is to constrain the physical conditions that give rise to these features, as well as to analyze the possible effects of artifacts in the

data reduction. In section 2 we describe briefly the modeling of spatially resolved spectra or position-velocity (PV) diagrams. The predictions and capabilities of our model are discussed in section 3. The comparison of theoretical single line diagrams with observations of HH 1F, HH 2(H+A′) and HH 43B, C is made in section 4. In section 5 we compare theoretical diagrams of line ratios and N_e with observations of HH 1+2. Our results are summarized in section 6.

2. Model

The kinematical model used in this study follows the approach of Raga & Böhm (1986) and HRH87. The bowshock is assumed to be axisymmetric of the form $x = {}^1/_2 r^2 + {}^1/_{10} r^4$ where x is the distance from the shock apex and r is the radius of the shock. This is the general bowshock form determined by HRH87. It is assumed that the thickness of the shock is negligible compared to the total shock dimension so that the emission originates from an infinitesimal shell. At each point on the shell, the perpendicular component of the shock velocity V_t is determined and the emission at that point is taken to be that of a plane-parallel shock with velocity V_t. The emission of the shock is projected onto the spectrographic slit and integrated over the shock surface. The resulting PV diagram is convolved with a gaussian in the spectral dimension to simulate instrumental and thermal broadening and one in the spatial dimension to approximate the seeing.

The emission characteristics of planar shocks have been extensively modeled. We use the models of HRH87, and when necessary we interpolate as precisely as possible between the models at shock velocities between 20 km s^{-1} and 350 km s^{-1}. At the time of publication, these results were believed to be accurate to within 30% from comparison with other models. A comparison with a more recent model shows that while the absolute flux may not be fully accurate, the shape of the flux as a function of velocity, which determines

the morphology of the PV diagrams, is consistent between models. Given the observed parameters of HH objects (dominated by radiative shocks) we limited our models to shock velocities of $\leq$250 km s^{-1}.

We are also presenting PV diagrams of line ratios in order to compare them with the observations (Solf & Böhm 1991). Using standard forbidden line ratios (e.g. [S II]$\lambda\lambda$6716/6731), we have also produced PV diagrams of the electron density N_e and electron temperature T_e. We solve the 5-level atom for the N_e dependence of the [S II]$\lambda\lambda$6731/6716 line ratio and the T_e dependence of the [O III](λ4959+λ5007)/λ4363 and [N II](λ6548+λ6583)/λ5755 ratios. Transitional probabilities and collisional strengths are taken from Osterbrock 1989. PV diagrams were generated for each line, and divided pixelwise disregarding any value of the denominator less than 0.005, a constant comparable to the calculation error. The ratio diagram was then translated pixel by pixel into a diagram of N_e or T_e.

The modeling process was thoroughly tested for error and artifact. Calculation error from the manipulation of the diagrams was determined to be negligible. The effects of increasing both the resolution of the output image and the resolution of the integration along the surface of the bowshock were studied, and changes in the final PV diagrams were found to be random and of very small magnitude. For presentation, the resolution of the PV diagrams of N_e and the line ratios was decreased by convolving a round gaussian with the image, of $\sigma = 1$ pixel. This corresponds to 5 km s^{-1} in velocity and 1/16 of the radius of the obstacle in position (for HH 1, this is $\simeq$0.″125).

3. Model Predictions

3.1. Predicted PV Diagrams for Single Lines and Line Ratios

A large portion of the model parameter space was explored. The plane-parallel shock models depend on preshock density (we use 100 cm^{-3}), chemical composition (we use solar), preshock magnetic field (we use $0.1\mu G$), and preionization. Models were generated for the full range of the shock velocity V, angle with the plane of the sky ϕ, and angle ξ between the shock axis and slit, for varying thermal and spatial widths using both equilibrium and full preionization. The PV diagrams for each line show the characteristic triangular shape, as well as the known double-peaked characteristics (for details see e.g. Raga & Böhm 1985, 1986). The diagrams tend to become shorter and have less of a high-velocity component (the "head" looks rounder) as ξ increases, naturally as less of the shock is in view of the slit. Diagrams also become shortened and increasingly asymmetric as ϕ increases. As velocity increases, the diagrams have a larger tendency to display double peaks, and the [S II] diagrams develop a "dip" behind the "head" at $V \simeq 100$ km s^{-1}. In Figure 1 we present PV diagrams for [CI]λ9850, [SII]$\lambda\lambda$ 6717+31, Hα, [OI]$\lambda\lambda$ 6300+63 and [OIII]λ 5007 for parameters similar to those of HH 1 - 2 (see below).

Once the PV diagrams for single lines are obtained it is straightforward to generate diagrams for the line ratios. In Figure 2 we show the [OI]/[SII], [OI]/Hα and [OIII]/Hα line ratios, again for HH 1 - 2 parameters. A detailed comparison with the observations is found in section 4.

3.2. Predicted PV Diagrams for N_e and T_e

The previously unexplored variation of N_e diagrams over this parameter space shows some strong characteristics similar to the variation of single line diagrams. As V increases (Fig. 3a), the PV diagrams simply become wider, and N_e remains constant as a function of velocity, as predicted by kinematic radiating bowshock models (Raga & Böhm 1985, 1986, HRH87, Solf & Böhm 1991). As ϕ increases (Fig. 3b), the PV diagrams become increasingly

asymmetric. The shape of this asymmetry is similar to that of the flux diagrams at the same value of ϕ, but the maximum of N_e tends to be at lower velocity than the maximum of flux. As ξ increases (Fig. 3c), the PV diagrams of N_e develop a dip in the central, low velocity area, and show double peaks at high velocity.

PV diagrams of T_e are calculated to further test the model, although no observed PV diagrams have yet been published. We again solve the 5-level atom, here for the temperature dependence of the [N II](λ6548+λ6583)/λ5755 ratio. As stated in section 2, the features of a PV diagram are a direct result of how the quantity (flux, N_e, T_e) shown in the diagram varies with velocity, as calculated for the plane-parallel shocks. T_e calculated for planar shocks from the [N II](λ6548+λ6583)/λ5755 ratio has a local maximum at $V \simeq 50$ km s^{-1} and a local minimum at $V \simeq 100$ km s^{-1}. This variation yields PV diagrams with features quite different from those of flux or N_e. Two maxima in T_e appear behind the shock "head", and not only is the first maximum some distance behind the leading surface of the shock, but the second maximum is sometimes larger than the first. Not only does the first rise in T_e not occur immediately behind the shock "head", but a second rise in T_e seems to occur further behind the shock "head", sometimes reaching larger values than the first maximum. The variation of the [O III](λ4959+λ5007)/λ4363 ratio and resulting T_e for planar shocks is identical in shape to the variation of the [N II](λ6548+λ6583)/λ5755 ratio, and thus the PV diagrams have the same features. Observed PV diagrams of T_e have not been published, but T_e calculated from integrated flux showing only spatial variation shows a double-peaked feature in both observation (Solf, Böhm, & Raga 1988) and this model.

4. Comparison with Observed Single Emission Lines in Specific Objects

4.1. HH 1

HH 1 - 2 is a well studied Herbig-Haro object. It is especially convenient because it is the brightest in the sky and the direction of the flow lies almost exactly in the plane of the sky. Figure 1 shows observations of HH 1 (first column) and HH 2 (third column) taken in various lines (Solf & Böhm 1991). The estimated thermal and instrumental broadening was 55 km s^{-1}, and the seeing $\simeq 1''$. In the models we have used gaussian functions in velocity and space with dispersions chosen to match these values. For the spatial smoothing, in particular, we use 1/2 of the radius of the "obstacle" causing the bowshock. For HH 1F, for instance, this value is estimated to be $\simeq 1''$ in size (Noriega-Crespo, Böhm, & Raga 1990).

Table 1 shows the shock characteristics which best match the observations (V=175 km s^{-1}, angle with respect to the plane of the sky ϕ=5±10, and slit angle ξ=0±10), and Figure 1 the corresponding theoretical PV diagrams (models of HH 1 in the second column and of HH 2 in the fourth). It is clear that the main condensation of HH 1 can be modeled well as a single bowshock traveling in the plane of the sky at moderate velocity.

Models generated using planar shock models with equilibrium preionization were qualitatively closer to observations than were models generated using full preionization. In observed PV diagrams, a flat tail one or two contour levels below the peak emission is often observed, especially in [S II] and [O I] lines. This feature can be reproduced theoretically using equilibrium preionization, but is not present in fully preionized models except in the H_α line. A common feature of all theoretical PV diagrams is that they tend to show more of a double peak than do diagrams derived from observation. This aspect of bowshock models has been examined before (Raga & Böhm 1985,1986) and its absence could be explained by a larger seeing or thermal broadening. It is important to note that although all models show more of a bimodal line profile than observation, the relative strength of the dip as different emission lines and shock parameters are compared seems to follow observation, e.g. the [O III] line shows a broader profile than the [S II] line in both observation and models.

Agreement of the theoretical results with observation is good for the [S II] $\lambda\lambda$6716+6731, [O I] $\lambda\lambda$6300+6363, and [O III] $\lambda\lambda$4959+5007 lines (all pairs coadded). Results are not as convincing for [C I] $\lambda\lambda$9823+9849 line, a deviation observed in previous models (Noriega-Crespo, Böhm & Raga 1990). The H_α line proved to be more difficult to model correctly. While emission in the tail of the shock decreases fairly rapidly, indicative of a reasonably low or (equilibrium) preionization state, the line profile at the "head" of a shock with equilibrium preionization is overly bimodal and diagrams generated using fully preionized shocks match the observed features more closely. We believe that neither full nor equilibrium preionization correctly models the preshock conditions near HH 1, and that this is especially apparent in this velocity range (170-190 km s^{-1}), where equilibrium shocks are becoming fully preionized.

4.2. HH 2

The morphology of HH 2 is more complicated than that of HH 1, and made of several more condensations (Schwartz et al. 1993). Two of the brightest ones are H and A′. Numerical models indicate that the working surfaces of jets can break into clumps due to Kelvin-Helmholtz and Rayleigh-Taylor instabilities (see e.g. Blondin et al. 1989). Once the working surface is broken the individual condensations interact by themselves with the interstellar medium. In the case of HH 2 the emission of each condensation can be modeled by individual bowshocks (see e.g. Hartmann and Raymond 1984). Based on the PV diagram appearance of the HH 2(H+A′), we model it as a superposition of two successive bowshocks, by simply adding the PV diagrams obtained from single bowshocks. Figure 1 shows the remarkable similarity with the observations.

Some important features are the slight asymmetry of the second shock (HH 2A′) and the roundness of the "head" of HH 2H. These result from the orientation of the bowshock:

HH 2A′ is best modeled using a shock traveling somewhat out of the plane of the sky ($\phi \simeq 12°$, which produces the asymmetry, and HH 2H is best modeled using a shock whose axis of motion is somewhat deviant from the slit angle ($\xi \simeq 35°$ — see Table 1). This large value of ξ is not unreasonable considering that the slit was not centered on HH 2H in these observations (Solf & Böhm 1991).

4.3. HH 43

HH 43 is a low excitation Herbig-Haro object in which the presence of several condensations again suggests two superimposed bowshocks. It is believed from analysis of the excitation and radial velocity of these regions that the shock velocity V and radial velocity V_r are small ($V \lesssim 50$ km s^{-1}, $V_r \simeq 25$ for HH 43C and $V_r \simeq 30$ km s^{-1} for HH 43B) (Böhm & Solf 1990). Planar shock data from HRH87 is sparse in this velocity regime and the error is believed to be high. We ran several planar shock models at low preionization and velocity (Table 2), which for [S II] $\lambda\lambda$6716, 6731 conforms with HRH87. We determined that $V \simeq 40$ km s^{-1} for HH 43B and $V \simeq 35$ km s^{-1} for HH 43C. Shock parameters best modeling the observations are shown in Table 1 and a comparison of observational and best fit theoretical PV diagrams is shown in Figure 4. Clearly, even in this low velocity regime, where planar shock models are less accurate, this kinematical model can reproduce many of the features of observed HH objects. Notable are the slight asymmetries of the maximum contour and the relative height of the maxima at the "head" of each shock.

5. Comparison of Line Ratios and Density Diagrams with Observation.

PV diagrams of line ratios and of N_e, determined from the [S II]λ6716/λ6731 ratio, provide more information and therefore can be more sensitive to shock parameters than PV

diagrams of the lines themselves. For HH 1 and 2, we have generated PV diagrams for the ratios [O I]/H_α, [O I]/[S II], [S II]/H_α, H_α/[S II], and [O III]/H_α, and for N_e. Many of the features of the ratios can be matched quite well by the kinematical bowshock models. Other diagrams, most notably N_e in HH 1, can only be explained by introducing a misalignment artifact, described below. Using the correct combination of physical parameters and this artifact, most of the remaining diagrams can be modeled.

A typical comparison of theoretical line ratio PV diagrams with observation is shown in Figure 2. All line ratios with the exception of [O III]/H_α show very low levels of structure, a feature which is present in the model as well. The evidence of some structure in the ratios with H_α is due to the fact that H_α is less well modeled by this simple model than are the other emission lines, as discussed above. The observed double peak in the [O III]/H_α ratios, due to the fact that the [O III] line has larger velocity dispersion than the hydrogen lines, is present in the model or HH 2, though not as strong as in the observations, and apparently missing in the model of HH 1.

As described above, a PV diagram of electron density N_e can be calculated from the ratio [S II]λ6716/λ6731. These diagrams often show important structure. Figure 5 shows the observed and theoretical PV diagrams of N_e for HH 2. Clearly, the model works well to explain many features of this detailed diagram. Note the single wide peak constant as a function of velocity present in HH 2H, the dip in N_e between the 2 condensations, the higher, double-peaked profile of HH 2A$'$, and even the slightly double-peaked profile behind the second shock, trailing off after a short distance

In the analysis of theoretical line ratio diagrams we discovered that a misalignment effect must be used to model certain lines. This effect has important implications for the correct analysis of observation because it can cause changes in PV diagram morphology which are stronger than those which result from the physical shock parameters. In

calculating PV diagrams of line ratios from observation, the PV diagrams of each line must be properly aligned, hence a judgement must be made about the center of the two line diagrams. Error in the spatial direction, along the slit, is expected to be small, but a shift on the order of several km s^{-1} in the spectral or velocity direction is not unreasonable. One can think of various sources of noise which would make determining the point of zero velocity on an observed PV diagram difficult. Using this model, the effects of misalignment of the two lines can be tested, since the exact center of each diagram is known. Figure 6 shows a PV diagram for [O I]/[S II] in which the lines have been shifted by 2 km s^{-1}. It is evident that the asymmetry seen in the observed line ratio diagram could simply be due to a slight misalignment.

As HH 1 is known to be a less complex object than HH 2, the N_e features of which are well explained by our model, it is to be expected that N_e in HH 1 should be even better modeled. The center diagram of Figure 6 shows the N_e diagram for the physical parameters which best model HH 1, and the top diagram the observed N_e. Apparently many of the features of N_e in HH 1 are not well explained by the model. Changes in physical shock parameters (V,ϕ,ξ) have little effect. However, the bottom diagram of Figure 6 shows a PV diagram of N_e, with the same physical parameters, but with the two flux diagrams shifted 0.05 pixels (3.1×10^{-3} radii $\simeq 0\farcs003$) in the spatial direction and 0.2 pixels (1 km s^{-1}) in the velocity direction relative to one another. Many features, including the asymmetric maximum at high velocity near the apex of the bowshock, contours otherwise constant with velocity, and the appearance of smaller maxima at some distance behind the "head" of the shock, along the edge of maximum velocity, are reproduced. It is important to note that the correct physical parameters as determined from matching PV diagrams of flux are still required to reproduce these features — N_e in HH 1 can only be modeled convincingly with the kinematical model by using *both* the best-fit physical parameters and a slight misalignment of the λ6731 and λ6716 diagrams. This is clear evidence that great care is

needed in interpretation of observed PV diagrams.

6. Conclusions

Model Predictions and Capabilities.— The kinematical model of bowshocks has proven useful to generate position-velocity (PV) diagrams of electron density N_e and electron temperature T_e as well as flux. A wide survey of the parameter space shows how PV diagram morphology varies with shock velocity V, the angle between the shock axis and the plane of the sky ϕ, the angle between the shock axis and the slit ξ, preionization state, thermal and instrumental broadening, and simulated seeing. The known features of flux PV diagrams (Raga & Böhm 1985, 1986) are confirmed and new features of N_e are demonstrated.

Comparison of flux diagrams with HH objects.— We have been able to determine theoretical shock parameters for several HH objects by matching the model PV diagrams with observed PV diagrams. We consider this method especially useful because the velocity information contained in PV diagrams allows rapid disqualification of large portions of parameter space, which might not be possible from examination of less detailed observations. We confirm that HH 1 can be modeled by a single bowshock moving nearly in the plane of the sky at $\simeq$175 km s^{-1}. We show that HH 2 can be modeled using two superimposed bowshocks with slightly differing directions: HH 2H nearly in the plane of the sky but not well aligned with the slit, $V \simeq$125 km s^{-1}, followed by HH 2A$'$ $\simeq 12°$ out of the plane of the sky and $\simeq 10°$ off the slit, $V \simeq$170 km s^{-1}. We also show the utility of the kinematical model in the less accurately modeled low velocity regime by modeling the low-excitation objects HH 43B,C as two superimposed bowshocks at $V \simeq$40 km s^{-1} and $V \simeq$35 km s^{-1}, respectively. We confirm the significant radial velocity of these objects, finding that ϕ is quite large for both.

Comparison with line ratios, N_e, and artifacts.— We have been able to use PV diagrams of line ratios to narrow the theoretical shock parameters for HH 1 - 2. Especially successful is the modeling of N_e in HH 2, in which most important features are reproduced by the model. We have also discovered that the proper alignment of the two diagrams to be divided is essential to properly observing physical characteristics of HH objects. We show that the asymmetric characteristics of ratios such as [O I]/[S II] could be the result of a slight misalignment. Finally, we show that many of the features of N_e observed in HH 1 are probably not physical, since in order to model them correctly using the kinematical model, small misalignments of the [S II] λ6716 and λ6731 lines are necessary.

R.I. and A.N.-C. thank Eileen Friel for her useful comments, and acknowledge the support by grants NSF-REU AST9300391 and the Perkin Fund (through MMO). A.N.-C. research is also supported by NASA Long Term Astrophysics Program (through IPAC). A.N.-C. thanks Karl-Heinz Böhm and Alex Raga for their encouragement to finish this project. We thank the referee for her/his careful reading of the manuscript and helpful suggestions.

REFERENCES

Blondin, J.M., Königl, A. & Fryxell, B.A. 1989, ApJ, 337, L37

Böhm, K.H., & Solf, J. 1990, ApJ, 348, 297

——-. 1992, AJ, 104, 1193

Choe, S.-U., Böhm, K.H., & Solf, J. 1985, ApJ, 288, 338

Curiel, S., Raymond, J.C. & Hartigan, P. 1994, ApJ(submitted)

Eislöffel, J., Mundt, R., & Böhm, K.H. 1994, AJ, 108, 1042

Hartmann, L. & Raymond, J.C. 1984, ApJ, 276, 560

Hartigan, P., 1989, ApJ, 339, 987

Hartigan, P., Raymond, J., & Hartmann, L. 1987, ApJ, 316, 323

Mundt, R. 1987, in IAU Symp. 122, Circumstellar matter, ed. I. Appenzeller & C. Jordan (Dordrecht; Reidel), 147

Noriega-Crespo, A., Böhm, K.H., & Raga, A.C. 1989, AJ, 98, 1388

——-. 1990, AJ, 99, 1918

Osterbrock, D.E. 1989, Astrophysics of Gaseous Nebulae and Active Galactic Nuclei (Mill Valley, CA: University Science Books)

Raga, A.C. 1988, ApJ, 335, 820

——-. 1994, in "Stellar and Circumstellar Astrophysics", ASPCS, 57, ed. George Wallerstein & Alberto Noriega-Crespo, 85

Raga, A.C. & Böhm, K.H. 1985, ApJS, 58, 201

——-. 1986, ApJ, 308, 829

Raga, A.C., Böhm, K.H., & Solf J. 1986, AJ, 92, 119

Raymond, J., 1979, ApJS, 39, 1

Schwartz, R.D. 1975, ApJ, 195, 631

Schwartz, R.D., Cohen, M., Jones, B.F., Böhm, K.-H., Raymond, J.C., Hartmann, L.W., Mundt, R., Dopita, M.A., & Schultz, A.S.B. 1993, AJ, 106, 740

Shu, F.H., Adams, F.C., & Lizano, S. 1987, ARA&A, 23

Smith, M.D., & Brand, P.W.J.L. 1990, MNRAS, 245, 108

Smith, M.D., Brand, P.W.J.L., & Moorhouse, A. 1991, MNRAS, 248, 451

Solf, J., Böhm, K.H., & Raga, A.C. 1988, ApJ, 334, 229

——-. 1986, ApJ, 305, 795

Solf, J., & Böhm, K.H. 1991, ApJ, 375, 618

This manuscript was prepared with the AAS LaTeX macros v3.0.

Table 1. Best fit Bow Shock Parameters

Model Parameter	HH 1F	HH 2H	HH 2A'	HH 43B	HH 43C
Thermal Width (km s^{-1})	28.5	28.5	28.5	60	60
Seeing (radii)	0.25	0.25	0.25	0.4	0.4
Shock Velocity V (km s^{-1})	175 ± 25	125 ± 15	170 ± 15	40 ± 5	35 ± 5
$\phi(°)$[a]	5 ± 10	2 ± 5	12 ± 5	55 ± 10	75 ± 5
$\xi(°)$[b]	0 ± 10	35 ± 10	10 ± 5	0 ± 25 [c]	0 ± 25 [c]

[a]Angle between shock velocity vector and plane of sky.

[b]Angle between shock velocity vector and slit.

[c]At low V, ξ makes only small differences in the PV diagram.

Table 2. Low Velocity Plane-Parallel Shock Data

Velocity (km s^{-1})	T_f[a] (K)	[S II]λ6716/ H_β	[S II]λ6731/ H_β	H_β (erg s^{-1} cm^{-2})
10.407	9000	3.73	2.54	3.551×10^{-5}
14.954	13000	2.94	2.01	1.289×10^{-3}
18.784	17000	52.7	36.1	6.374×10^{-3}
20.[b]	—	8.51	5.87	9.4×10^{-3}
21.258	20000	2.39	1.64	1.239×10^{-4}
30.[b]	—	2.09	1.51	6.7×10^{-2}
30.389	34000	1.60	1.15	9.508×10^{-4}

[a]final temperature behind shock

[b]HRH 1987

Figure 1. Observed (Solf & Böhm 1991) and theoretical diagrams of flux in various lines for HH 1 (first 2 columns) and HH 2 (third and fourth column). Adjacent contours represent a factor of 2 in the intensity. All but H_α represent coadded fluxes. i.e. [O I] $\lambda\lambda$6300+6363), [S II]$\lambda\lambda$6716+6731, [O III]$\lambda\lambda$4959+5007, and [C I]$\lambda\lambda$9823+9850.

Figure 2. Observed (Solf & Böhm 1991) and theoretical PV diagrams of line ratios for HH 1 - 2. Ratios are [O I]/[S II], [O I]/H_α, and [O III]/H_α. H_α is fully preionized. Successive contour lines represent a factor 2 change in the ratio. The lowest contour is 0.5 for the [O I]/[S II] ratio, 0.35 for the [O I]/H_α ratio, and 2 for the [O III]/H_β ratio (for both observed and theoretical diagrams).

Figure 3a. Theoretical N_e determined from [S II] $\lambda\lambda$6731/6716. Variation with shock velocity V. The "head" of the shocks are to the left. i.e. in the jet model, the jet is traveling left, or in the "shocked cloudlet" model, the wind is blowing to the right. Two successive contour lines correspond to a factor $\sqrt{2}$ in N_e and the lowest solid contour is $N_e = 50cm^{-3}$.

Figure 3b. Variation of N_e with ϕ (angle between shock axis and plane of sky).

Figure 3c. Variation of N_e with ξ (angle between projected shock axis and slit).

Figure 4. Observed (Solf & Böhm 1990) and theoretical PV diagrams for HH 43B & C in [S II]λ6716 and λ6731. Successive contours correspond to a factor 2 change in flux.

Figure 5. Observed (Solf & Böhm 1991) and theoretical PV diagrams of N_e in HH 2. Adjacent contour lines represent a change by a factor 2 in N_e. The lowest contour represents N_e =250 cm^{-3}.

Figure 6. PV diagrams of [O I]/H_α and N_e in HH 1. Observed, theoretical without misalignment and theoretical with misalignment. For [O I]/H_α, the misalignment is 2 km s^{-1}, and successive contours represent a factor 2 change in the ratio. The lowest contour in the observed diagrams and the lowest solid contour in the theoretical diagrams represents a value of 0.35. For N_e, the misalignment is 3.1×10^{-3} radii $\simeq$ 0.″003 in the spatial direction and 1 km s^{-1} in the velocity direction, successive contours represent a factor 1.59 change in N_e and the lowest contour represents N_e =250 cm^{-3}.

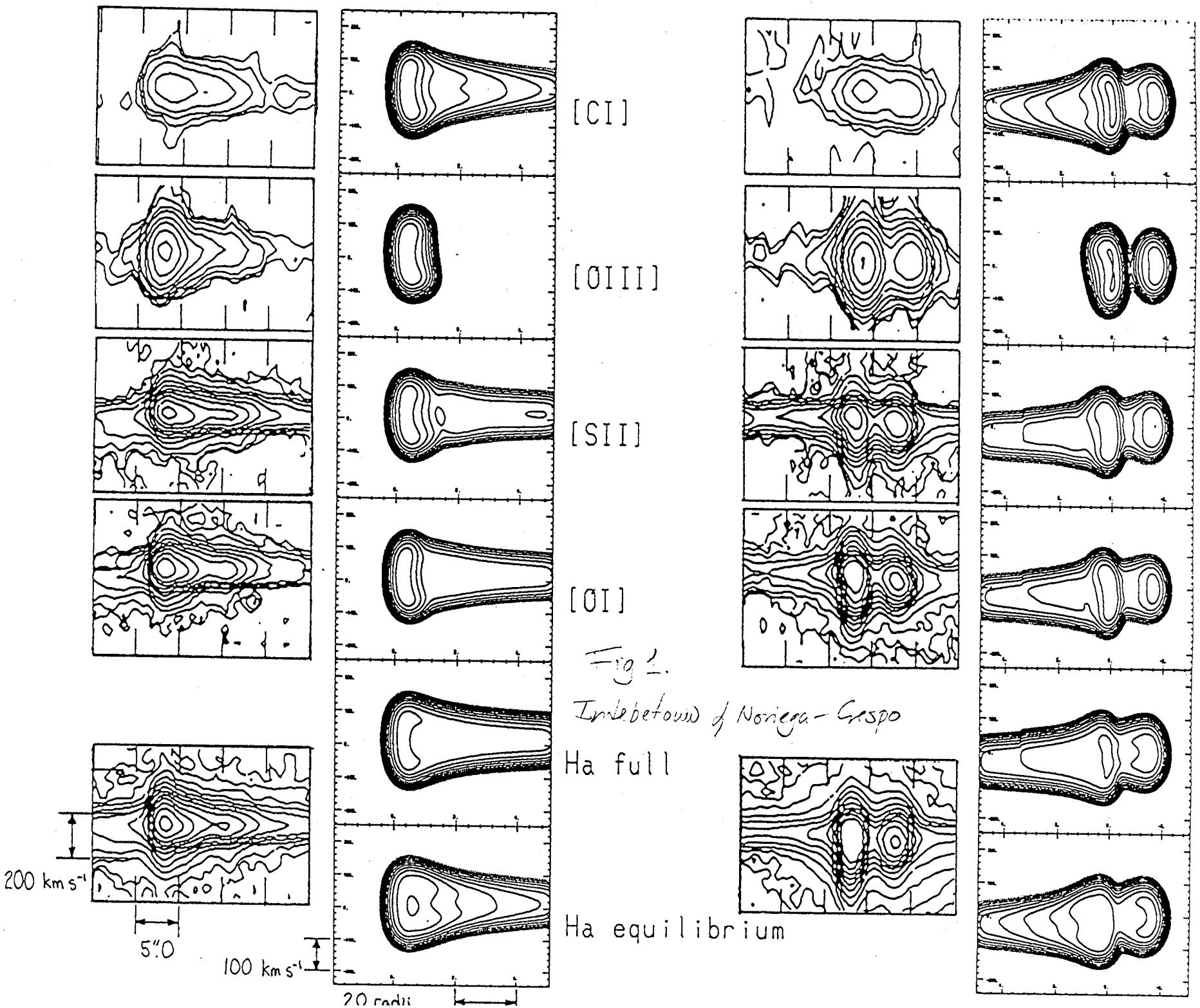

Fig 1.
Indebetouw of Noriega-Crespo

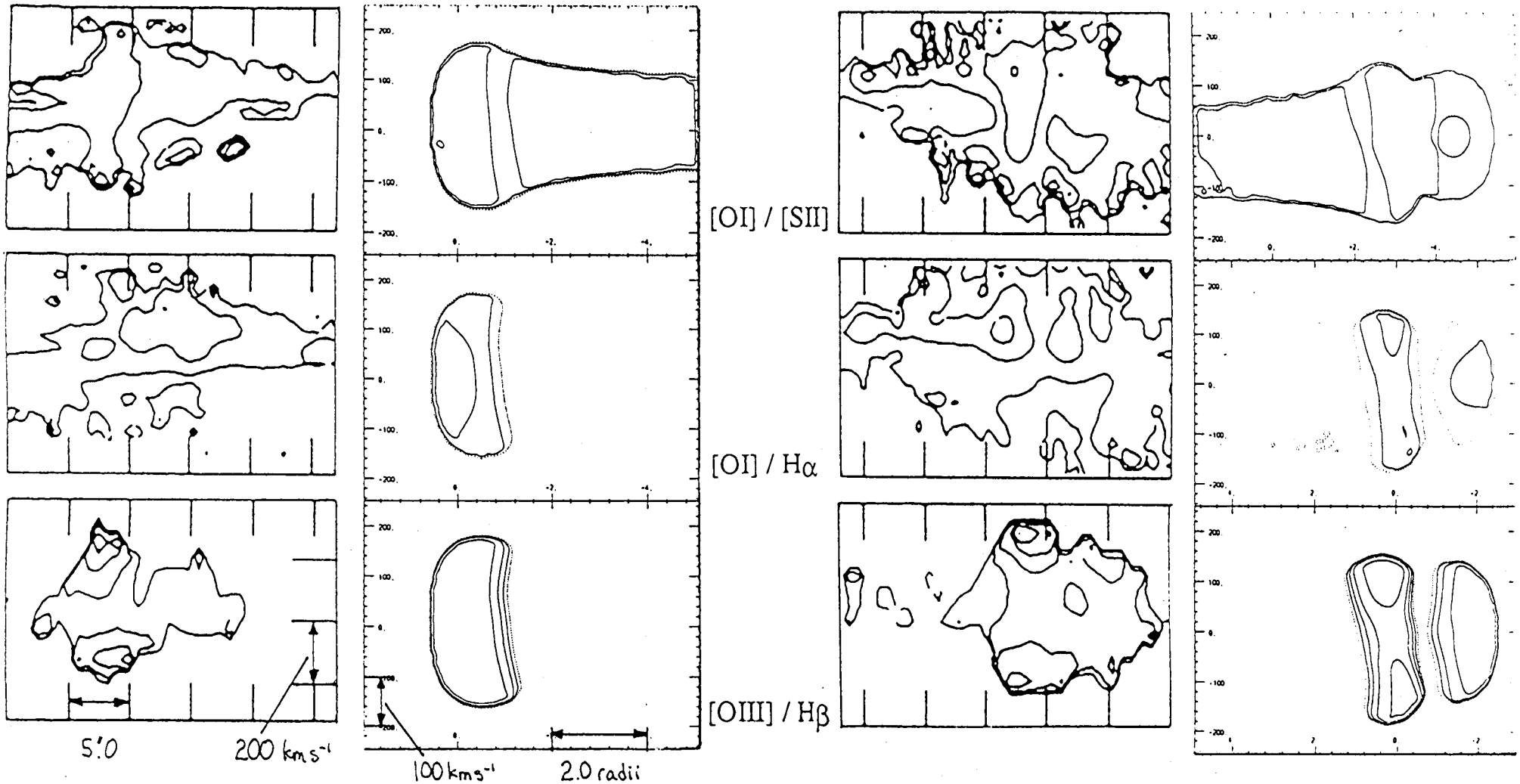

Fig 2

In debe-town of Noriega-Crespo

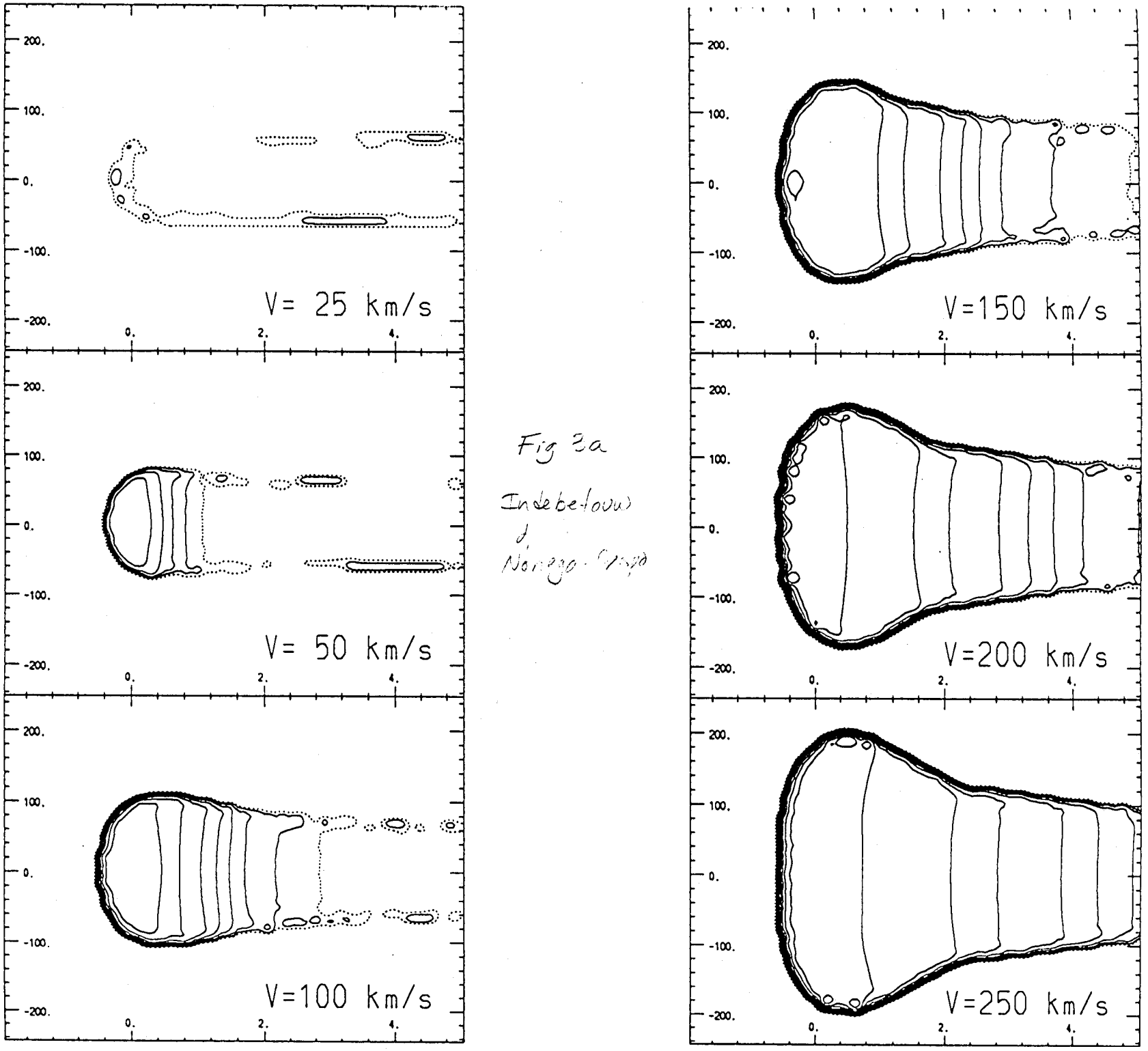

Fig 3a

Indebetouw
&
Nonega-Crespo

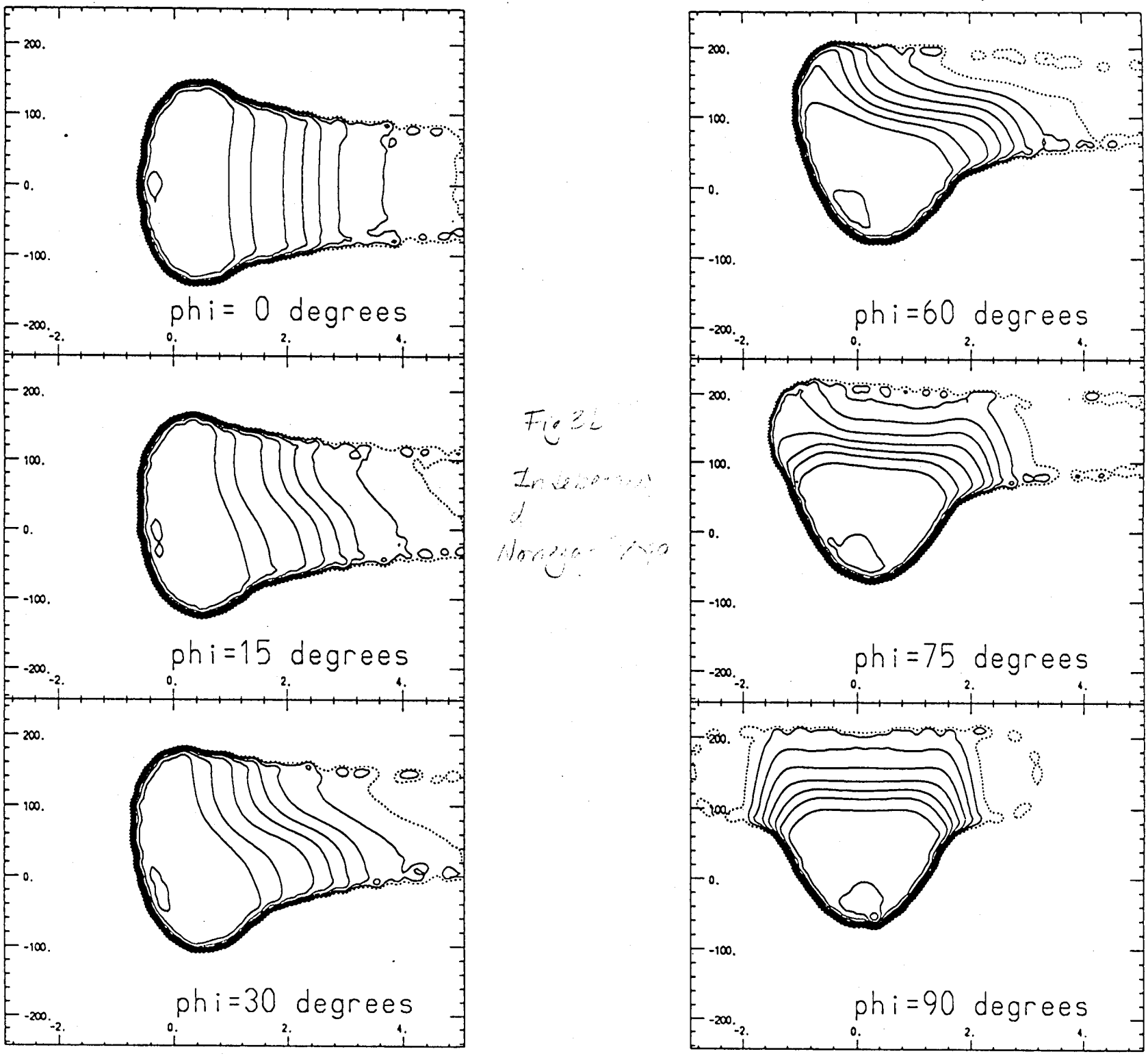

Fig 3b
Indeborow
&
Nonzyo-Yao

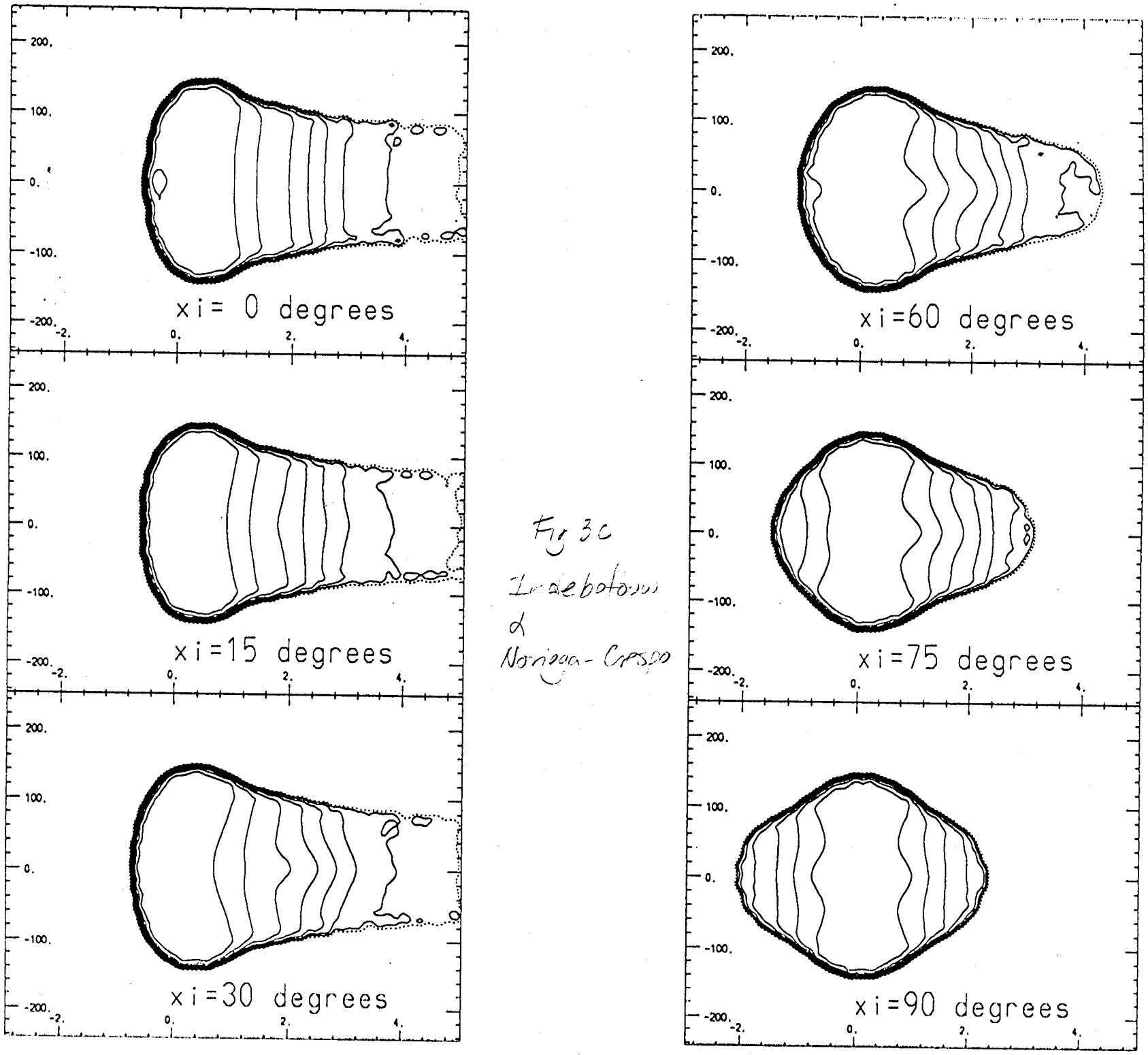

Fig 3c
Indebetouw
α
Noriega-Crespo

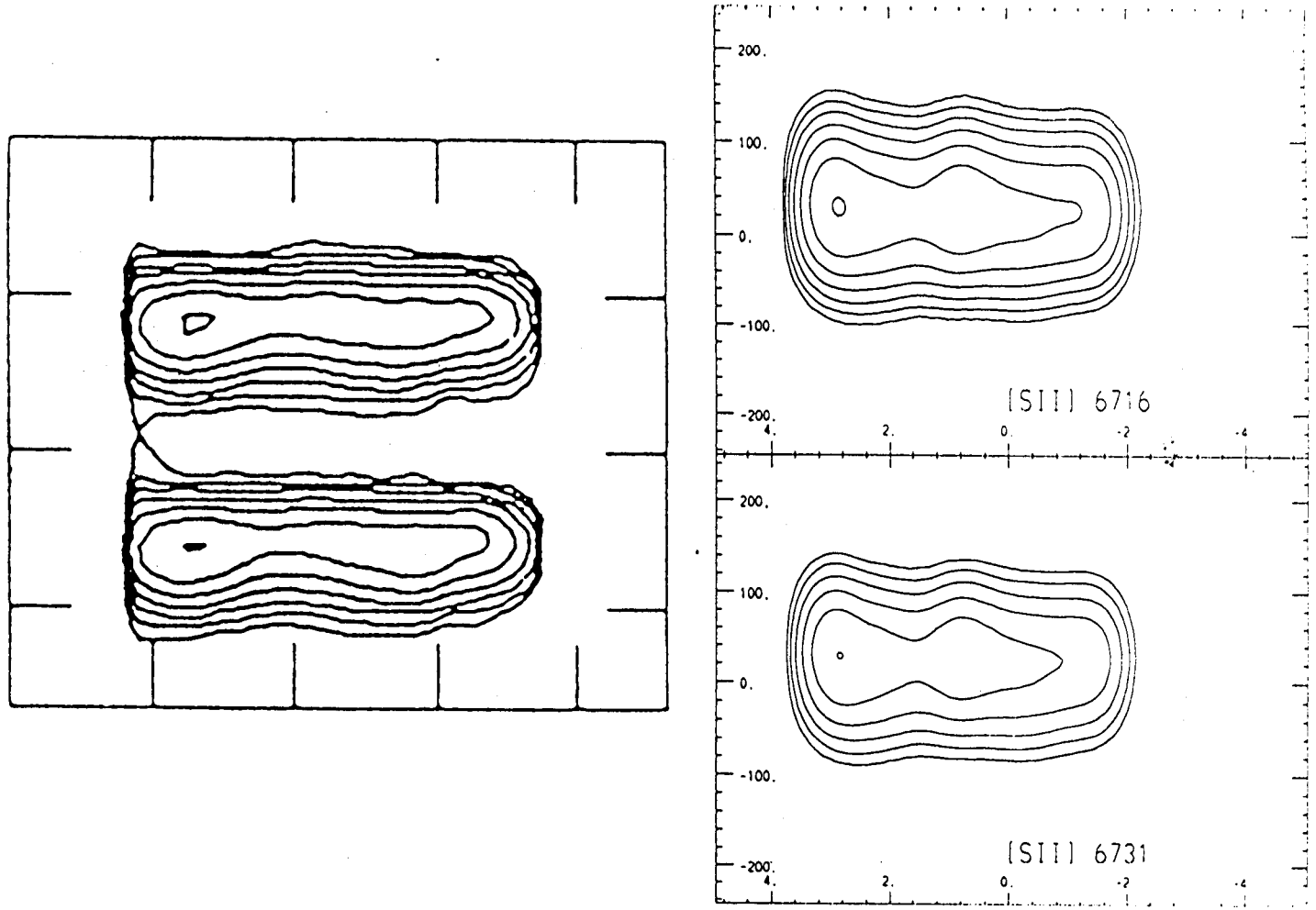

Fig 4.

Indebetouw of Noriega-Crespo

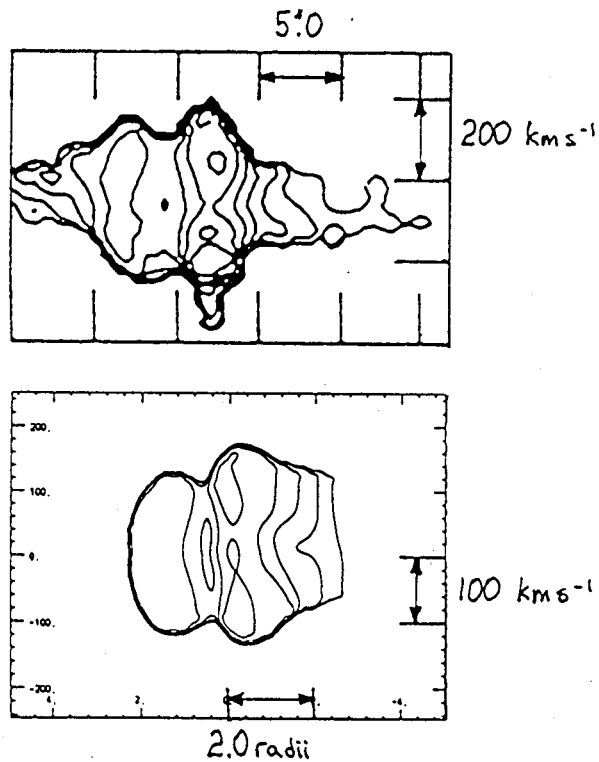

Fig 5
Indebetouw of Noriega-Crespo

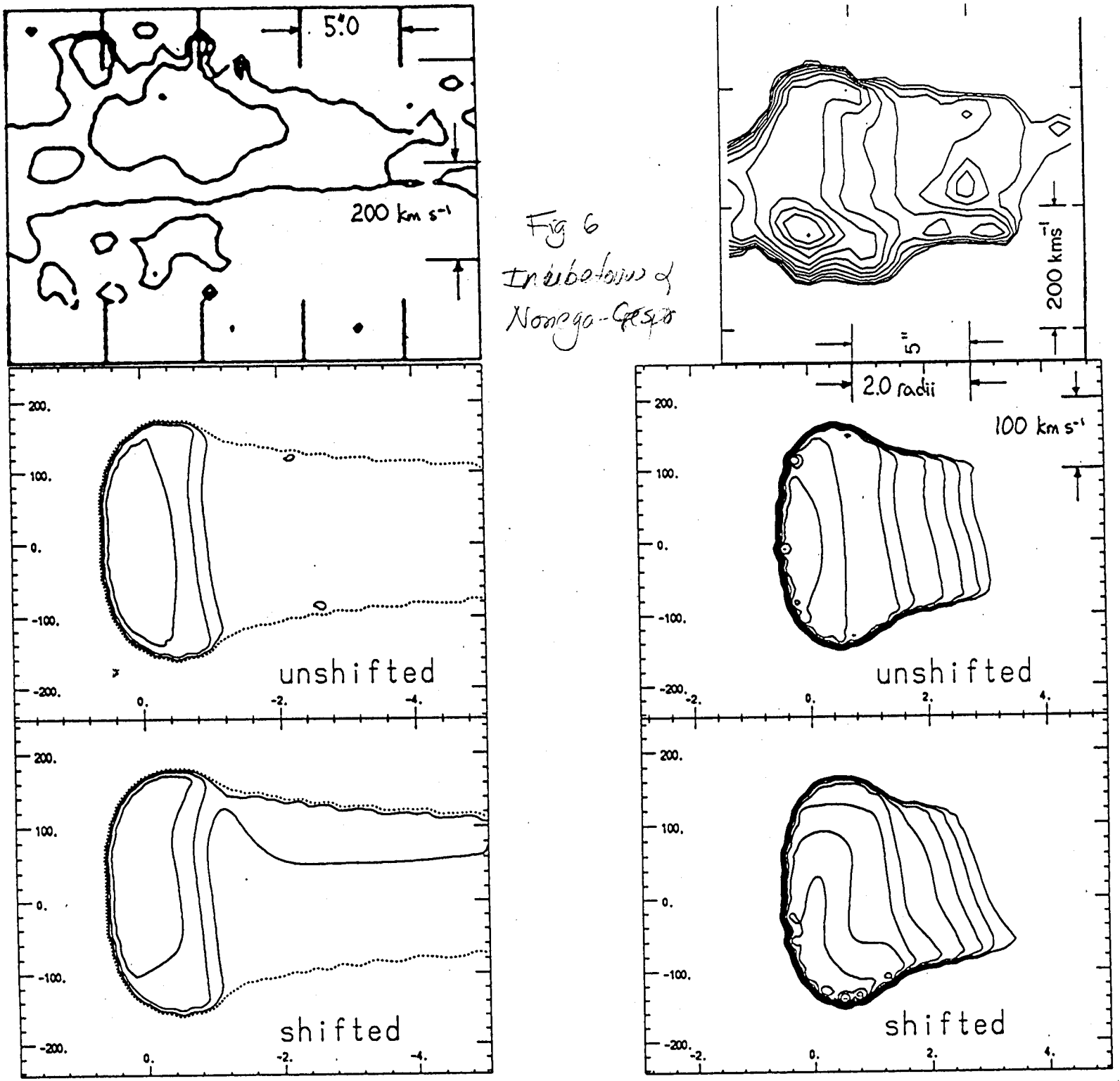

Fig 6
Indebetouw & Noriega-Gespo